Overpressured underthrust sediment in the Nankai Trough forearc inferred from high-frequency receiver function inversion

Takeshi Akuhara[1], Takeshi Tsuji[2], and Takashi Tonegawa[3]

[1] Earthquake Research Institute, The University of Tokyo

[2] Department of Earth Resources Engineering, Kyushu University

[3] Research Institute for Marine Geodynamics, JAMSTEC

Corresponding author: Takeshi Akuhara (akuhara@eri.u-tokyo.ac.jp)

Key Points:

- We applied transdimensional inversion of receiver function waveforms to seafloor cabled stations at the Nankai subduction zone.
- The resultant high-resolution velocity structures allow a direct comparison to active source surveys.
- A low-velocity zone beneath the outer ridge is evident, which is interpreted as an overpressured portion of underthrust sediment.

Abstract

Active-source seismic surveys have resolved the fine-scale P-wave velocity (Vp) of the subsurface structure in subduction forearcs. In contrast, the S-wave velocity (Vs) structure is poorly resolved despite its usefulness in understanding rock properties. This study estimates Vp and Vs structures of the Nankai Trough forearc, by applying transdimensional inversion to high-frequency receiver function waveforms. As a result, a thin (~1 km) low-velocity zone (LVZ) is evident at ~6 km depth beneath the sea level, which locates ~3 km seaward from the outer ridge. Based on its high Vp/Vs ratio (~2.5) and comparison to an existing seismic reflection profile, we conclude that this LVZ reflects a high pore pressure zone at the upper portion of the underthrust sediment. We infer that this overpressured underthrust sediment hosts slow earthquake activities, and that accompanied strain release helps impede coseismic rupture propagation further updip.

Plain Language Summary

Many geophysical surveys have investigated the subsurface structures of shallow subduction zones by estimating the propagation speed of compressional waves emitted from artificial explosive sources. Although shear and compressional wave speeds are necessary to understand rock properties (e.g., water content) of the subsurface, it has been difficult to constrain the shear wave speed with a high-resolution. In this study, we estimate both compressional and shear wave speeds by applying an advanced technique to earthquake waveforms recorded at ocean-bottom seismometers deployed at the Nankai subduction zone, Japan. The results show a sufficiently high spatial resolution to detect a thin (~1 km) layer, which we interpret as water-rich subducted sediment. This water-rich zone may promote slow slips on the megathrust fault and work as a barrier against rupture propagations during large earthquakes.

1 Introduction

Evaluating the pore fluid pressure distributions in the subduction margins is a key element to understand slip behaviors of the megathrust fault. At accretionary margins, unconsolidated sediment is accreted at the deformation front and further compacted by tectonic loading over time. During this process, abundant fluids are released from the sediment through mechanical compaction or metamorphic dehydration (J. C. Moore & Saffer, 2001). The released fluid can concentrate along nearby faults, and the elevated pore fluid pressure can weaken the fault strength by effectively reducing the normal stress (e.g., Scholz, 1998). Such a weakening mechanism has been suggested to affect the rupture propagation on the megathrust (e.g., Kimura et al., 2012) and contribute to the generation of slow earthquakes (Saffer & Wallace, 2015).

Active-source seismic surveys have been widely used to infer pore pressure distribution (e.g., Tsuji, Kamei, et al., 2014). High-resolution (~0.1–1 km) P-wave velocity (Vp) structure or reflection profiles have been acquired for many subduction zones (Bell et al., 2010; Canales et al., 2017; Gray et al., 2019; Kamei et al., 2012; Li et al., 2015; Shiraishi et al., 2019). In these studies, low Vp or highly reflective zones are often associated with high pore fluid pressure; however, interpreting rock properties from only Vp (or impedance) information is somewhat subjective. With independent estimates of S-wave velocity (Vs), one can acquire more robust constraints on pore fluid pressure (Dvorkin et al., 1999). Unfortunately, marine active-source surveys are not particularly sensitive to Vs.

In contrast to active-source surveys, passive-source analyses can be highly sensitive to Vs. The receiver function method (Langston, 1979) aims to retrieve the impulse response of the near-receiver structure, i.e., the Green functions (GFs), from teleseismic P coda by deconvolving incident source wavelet. The retrieved receiver function can then be inverted for the velocity structure beneath the receiver. Early studies used the method at low-frequency (< 1 Hz) to avoid numerical instability of the deconvolution. Later, many studies have improved the technique such that it can work with higher frequencies (e.g., Ligorría & Ammon, 1999), leading to higher spatial resolution (~1 km). Nevertheless, most receiver function methods fail to approximate GFs when calculated using data from ocean-bottom seismometers. This is due to intense water reverberations dominating the vertical component records. Recent efforts have overcome this difficulty and allowed for investigating subsurface structure using high-frequency receiver functions with data from offshore observatories (Akuhara et al., 2016, 2017, 2019).

This study performs the receiver function inversion for stations from the seafloor cabled network (DONET1) deployed at the Kumano-nada (Kumano Sea) in the central Nankai subduction zone. First, we calculate high-frequency receiver functions, or GFs, using the multichannel deconvolution (MCD) method (Akuhara et al., 2019). Then, the GFs are inverted for the one-dimensional (1-D) seismic velocity structure beneath each station using transdimensional Markov-chain Monte Carlo (MCMC) sampler (Green, 1995). Using this, one can solve an inverse problem without knowing the number of unknowns (i.e., the number of layers in the subsurface structure) a priori. This feature is advantageous for GFs at offshore sites, for which visual interpretation is challenging because of intense reverberatory phases at the sea surface, sea bottom, and sediment-basement interface.

The spatial resolution of the resulting velocity structure is sufficiently high to detect a thin (~1 km) low-velocity zone (LVZ) that is considered fluid-rich. By comparing the results to the seismic reflection profiles, we detect overpressured features in the Nankai Trough subduction forearc and discuss their implications on the earthquake process. We aim to highlight the advantage of high-resolution studies of Vs structure by receiver functions using offshore data. Future progressive passive-seismic observations at offshore regions can facilitate this class of study, leading to a better understanding of subduction processes.

2 Tectonic Setting and Seafloor Observatories

Kumano-nada is in the central Nankai subduction zone, where the Philippine Sea plate obliquely subducts beneath the trough margin (Figure 1a). Megathrust earthquakes repeatedly rupture the plate interface over a cycle of ~100–150 years (Ando, 1975), including the 1944 Tonankai earthquake (Figure 1a, magenta contour). Because of the imminent risk of future megathrust earthquakes, the area's subsurface structure has been intensively investigated by active-source surveys (e.g., Bangs et al., 2009; Kamei et al., 2012; G. F. Moore et al., 2009; Nakanishi et al., 2008; Park et al., 2002). The accretionary prism developed at the margin can be divided into outer and inner wedges. The transition between these two zones is characterized by the outer ridge, splay fault, and strike-slip fault (Figure 1b). All of these features are dominant and thus can be seen along the entire forearc (Tsuji, Ashi, et al., 2014).

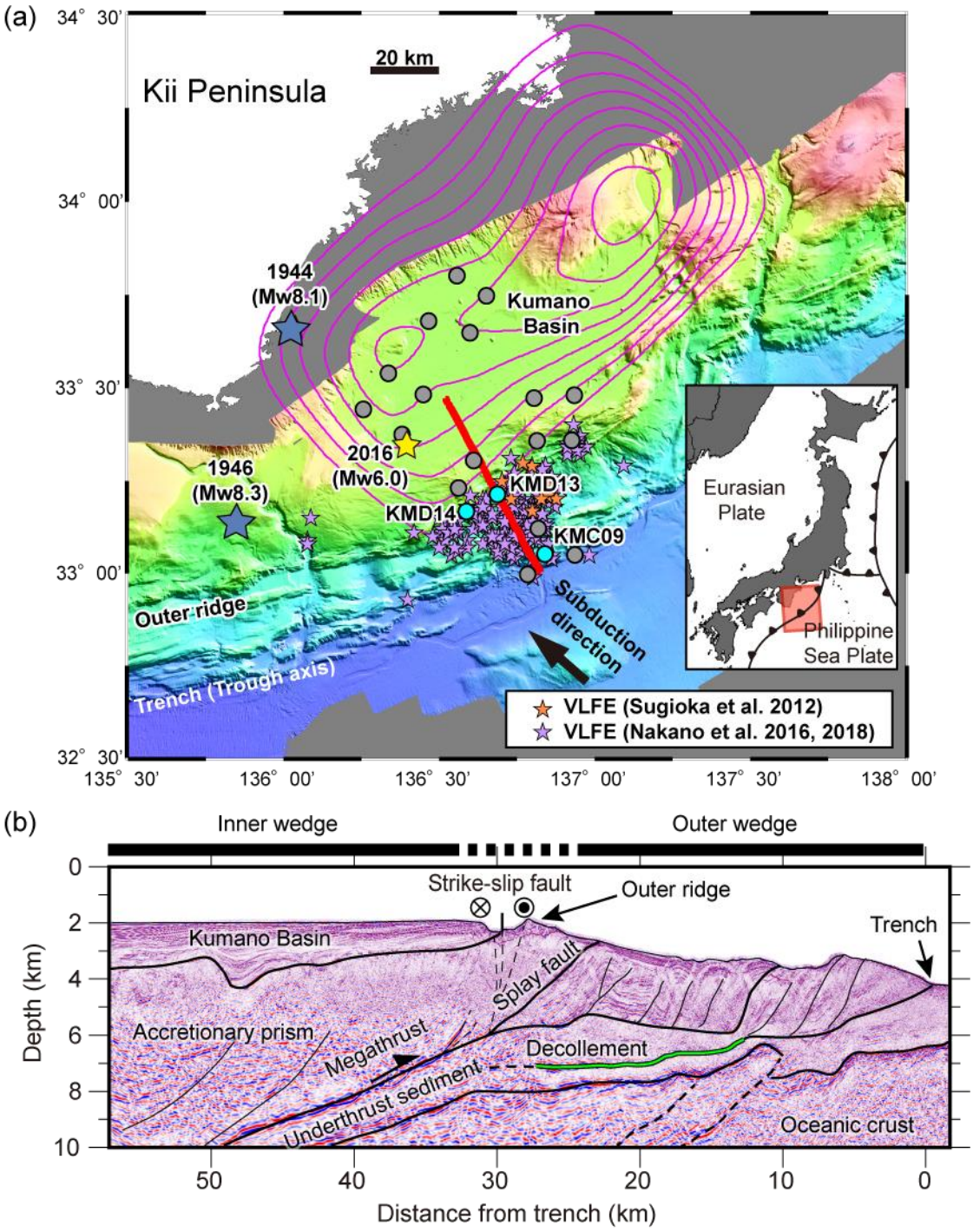

Figure 1 (a) Tectonic setting of the study area. Circles denote the seafloor cabled seismometer network (DONET1). The stations used in this study are colored in sky blue. The bold red line indicates the location of the seismic reflection profile shown in (b). Orange and purple stars denote epicenters of very low-frequency earthquakes (Nakano et al., 2016, 2018; Sugioka et al., 2012). The magenta contour shows coseismic slip distribution during the 1944 Tonankai Earthquake with an interval of 0.5 m (Kikuchi et al., 2003). **(b)** Seismic reflection profile crossing the study area and its interpretation after Tsuji, Kamei, et al. (2014).

Despite the progressive surveys, geological interpretation near the plate boundary remains under debate, even for the shallower portion (i.e., the trenchward side of the outer ridge). Early works interpreted a strong horizontal reflective surface (Figure 1b, green horizontal line) as the plate boundary fault (Park et al., 2002), often termed a "décollement". Later, a three-dimensional prestack migration study (Park et al., 2010) detected an LVZ ~2 km in thickness immediately above the décollement (Figure S1) and interpreted it as antiformal stacking of the underthrust sediments. However, the downdip continuation of this LVZ was unclear because of the limited resolution at depth. Subsequently, full-waveform inversion studies (Kamei et al., 2012, 2013) have shown that the LVZ extends further downdip to ~10 km depth (Figure S1). Tsuji, Kamei, et al. (2014) interpreted this LVZ as an overpressured shear zone and suggested it as the location of megathrust faulting. Although the true "thrust" location remains unclear, we use the term "underthrust" sediment to refer to this LVZ. It should be reminded here that all studies mentioned above are on the basis of Vp information.

The seafloor cable seismometer network, DONET1, has shown a wideband of transient slips (i.e., slow earthquakes) occurring in this region, including very-low-frequency earthquakes (VLFEs), low-frequency tremors, and slow slip events (Araki et al., 2017; Nakano et al., 2018; Takemura et al., 2018; To et al., 2015). These epicenters are located updip of the seismically locked zone where the 1944 Tonankai earthquake ruptured. They have been considered to occur either on the plate boundary fault or the splay fault within the accretionary prism; this is still an open question because of the difficulty in obtaining reasonable constraints on their focal depths. Lines of evidence suggest that the generation of these slow earthquakes is owing to high pore pressure (Ito & Obara, 2006; Kitajima & Saffer, 2012; Tonegawa et al., 2017).

This study mainly focuses on the two DONET1 stations located close to the seismic reflection profile: one is near the deformation front (KMC09), and the other is near the outer ridge (KMD13). We additionally use the data from the station KMD14 to highlight the structural feature obtained near the outer ridge.

3 Method

We retrieve the radial component GFs from teleseismic P waveforms using the MCD technique. This extended receiver function method can be reasonably applied to offshore data contaminated by intense multiples from the water column (Akuhara et al., 2019). The detailed processes are as follows. First, we select teleseismic events that occur from November 1st, 2014, to June 19th, 2019, with M>5.5 and epicentral distances of 30–90˚. The seismic waveforms of these are then rotated to the radial-transverse-vertical coordinate system. We measure the signal-to-noise (SNR) ratio, which we define by the root-mean-square amplitude ratio of 30 s windows before and after the P arrival, on vertical component records. The records with an SNR>2.5 are retained and processed by the MCD. During the deconvolution, a Gaussian low-pass filter ($\mathcal{G}(\omega) = \exp\left(-\frac{\omega^2}{4a^2}\right)$) with a parameter a=8.0 is applied. The upper-frequency limit is ~3.8 Hz, at which the filter gain falls to 10% of the maximum. Both radial and vertical component records are used as inputs to the MCD, which results in GF estimations for both components. In this study, we only focus on the radial components as the first step.

Because of the laterally heterogeneous structure in the study region, resultant GFs vary in response to incoming ray directions, or event back-azimuths. To avoid this complexity, we

divide all GF traces into two subsets (updip or downdip datasets) depending on the incoming direction relative to the subducting plate. For each subset, we calculate cross-correlation coefficients (CCs) between all pairs of GFs and select GFs that show high coherency (CC>0.65) with at least half of all GFs within the subset (Figure S2). GFs satisfying this condition are stacked and used as input data for the following inversion analysis. We carry out the inversion analysis separately for each updip and downdip data, leading to two independent results per station.

We employ transdimensional MCMC inversion (e.g., Agostinetti & Malinverno, 2010; Bodin et al., 2012) for solving seismic velocity structures. We assume an isotropic layered medium beneath the seafloor (i.e., the station level) and express the structure using the following unknowns: the number of layer interfaces (k), their depths (z_i, $i = 1 \cdots k$), and the P and S-wave velocity anomalies ($\delta\alpha_i$ and $\delta\beta_i$, $i = 1 \cdots k+1$). These velocity anomalies are defined relative to the station-specific reference velocity models estimated by Tonegawa et al. (2017). These velocity models are determined from Rayleigh wave admittance, a ratio of the vertical displacement to the pressure on the seafloor (Ruan et al., 2014), offering a reasonable constraint on Vs. The densities are scaled to Vp by an empirical relation (Brocher, 2005). The properties of the ocean layer are fixed as follows: Vp and density are assumed to be 1.5 km/s and 1.0 g/cm^3, respectively, and the station level is used for the thickness. Although there are some reports of anisotropy in the study region (Tsuji et al., 2011), we limit our analysis to the isotropic case for simplicity.

The posterior probability in terms of k, z_i, $\delta\alpha_i$, and $\delta\beta_i$, which is proportional to the prior-likelihood product, is sampled by the reversible-jump MCMC algorithm (Green, 1995). The method explores multidimensional model space via random walks (i.e., perturbing z_i, $\delta\alpha_i$, and $\delta\beta_i$), together with the random increase/decrease in the model space dimension (i.e., increasing/decreasing k). We assume truncated uniform priors for k and z_i and zero-mean Gaussian priors for $\delta\alpha_i$ and $\delta\beta_i$. Besides these priors, we prohibit anomalous layers with either too high/low velocities or Vp/Vs. We employ the propagator matrix method (Thomson, 1950) for the forward computation, and then the likelihood is calculated in the manner that can consider a temporal correlation of data noise (Bodin et al., 2012). A parallel tempering method (Sambridge, 2014) is adopted to increase the conversion rate of the inversion. See Text S1 for more details of the MCMC inversion.

The models sampled by the MCMC construct the posterior probability distribution, from which any derivatives, including marginal probability, mean model, or confidence interval, can be drawn. Recall that we obtain two independent probability distributions per station derived from the updip and downdip datasets. Comparing these results may provide useful insight into lateral heterogeneity. In our results, however, the difference is found to be negligible, with an exception discussed later. In the following section, we report confidence intervals of Vs and Vp/Vs that are calculated by simply merging the two results.

4 Results and Interpretations

The inverted velocity structure for the site close to the trench (KMC09) shows two thin (< 2 km) layers immediately beneath the seafloor (Figures 2a-d, S3). The 95% confidence intervals of Vs and Vp/Vs for the upper layer are 0.5–0.8 km/s and 3.2–4.3, respectively, while

198 the lower layer exhibits 0.9–1.8 km/s and 1.8–3.4. Comparing to the seismic reflection profile,
199 we interpret these layers as the incoming sediment overlaid by the accreted sediment (Figure 3).
200 The extremely low Vs and high Vp/Vs indicate the unconsolidated nature of the sediment. Such
201 a high Vp/Vs of the sediment near the deformation front is also inferred from a refraction survey
202 using converted phases (Tsuji et al., 2011). The sharp drop in Vp/Vs to < 2.0 at 6.5 km depth
203 well defines the sediment-oceanic crust interface and closely matches the reflective band seen in
204 the profile of Figure 3. Vs at the top of the oceanic crust is estimated to be ~ 2.5 km/s, which is
205 expected for the basaltic layer known as oceanic layer 2 (Christensen, 1978). The velocity
206 gradually increases with depth to ~4.8 km/s at 10 km depth, considered as the gabbroic oceanic
207 crust (oceanic layer 3).

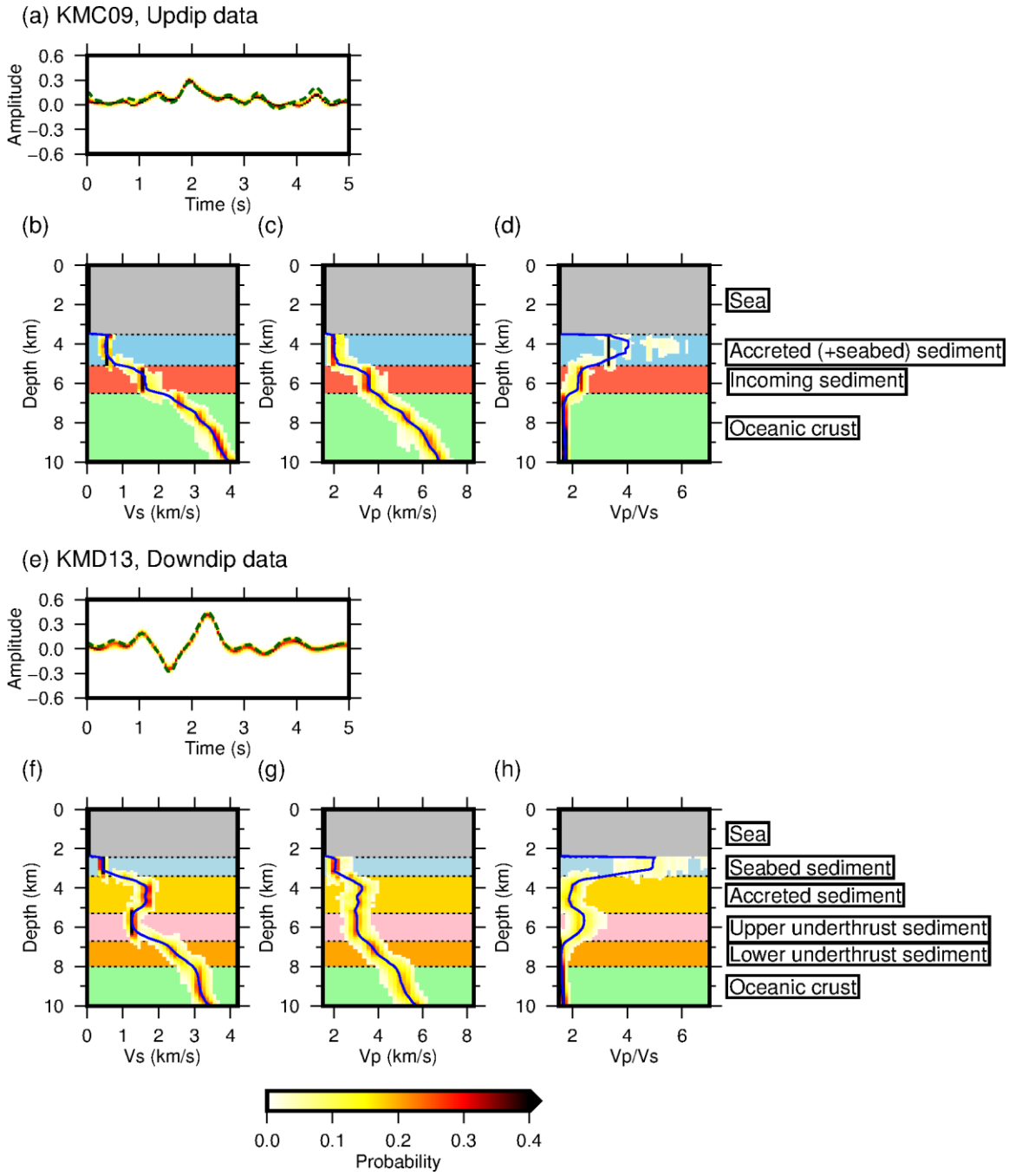

Figure 2 Results of inversion analysis for (a-d) KMC09 and (e-h) KMD13. (a, e) Input Green's functions (green dashed line) and the frequency distribution of predicted Green's functions (red and yellow gradation). (b-d, f-h) Posterior marginal probability distributions of (b, f) Vs, (c, g), Vp, and (d, h) Vp/Vs structures (red and yellow gradation). Note that negligible probability (< 0.01) is muted. The blue lines represent the mean models. The background color shows the geological interpretation.

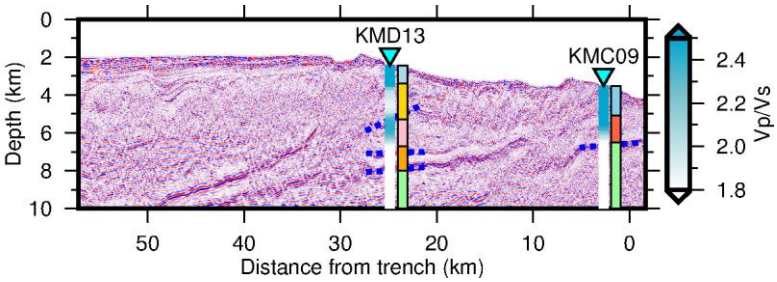

Figure 3 Comparison of Vp/Vs to the seismic reflection profile. The bluish color shows Vp/Vs (i.e., the mean model) estimated by this study. Colored rectangles indicate the geological interpretation with the same color notation as Figure 2. The blud doted line segments highlight reflective bands that agree with our interpretation.

The inverted velocity structure near the outer ridge (KMD13) can be divided into five geological units: the seedbed sediment, accreted sediment, upper underthrust sediment, lower underthrust sediment, and oceanic crust (Figures 2e-h and S4). Note that we define these boundaries by discontinuities in Vs or Vp/Vs, but they are mostly consistent with the reflective band seen in the reflection profile (Figure 3). Remarkably, the upper underthrust sediment exhibits lower Vs (with a 95% confidence interval of 1.1–1.6 km/s) and higher Vp/Vs (1.9–2.9) than above it. The stratification of marine sediments typically shows the highest Vp/Vs at its top, and the ratio decreases with depth because of the increase in effective stress (e.g., Hamilton, 1979). The higher Vp/Vs than that of the shallower part, as seen here, can be explained by elevated pore pressure (Dvorkin et al., 1999). Note that the low Vs obtained is essential here because the low Vp can be explained by gas saturation in addition to high pore pressure. The lower underthrust sediment shows distinguishably higher Vs (or lower Vp/Vs) compared to the upper underthrust sediment. The sharp Vs contrast is most likely to correspond to the décollement interpreted on the reflection profile (Figures 1b and 3). We, therefore, conclude that fluid is confined in the volume between the décollement and the base of accreted sediment.

We notice that the low-velocity feature for the upper underthrust sediment is not clear in the results form the updip data (Figure S4). This may be due to the effect of a dipping layer. The incident angle to the dipping layer is smaller for ray paths from the updip direction, leading to less efficient P-to-S conversions at the interface. Indeed, the top-surface of the underthrust sediment indicates a steeper dip angle than the décollement and the top of the oceanic crust (Figure 3). Reasonable treatment for this dipping effect will improve the Vs estimation for this layer, which is left for our future work. Additional inversion analysis on KMD14, which locates in a similar tectonic setting, provides another supportive evidence. The result shows a similar pattern to KMD13 in that it consists of the same five geological units with comparable velocities (Figure S5).

5 Discussion and Conclusions

We estimated 1-D seismic velocity (Vp and Vs) structures beneath the DONET1 stations, located in the center of the Nankai subduction zone, using transdimensional MCMC inversion. The high-frequency content (up to ~3.8 Hz) of the input waveforms offers a high spatial resolution sufficient for a direct comparison to the seismic reflection profile. Regarding a high Vp/Vs as an indicator of high pore pressure, we detected fluid-rich features in the forearc margin

(Figure 4). At the onset of the subduction (KMC09), both incoming and accreted sediments indicate the mean Vp/Vs higher than 2, indicative of the unconsolidated nature. Near the outer ridge (KMD13), Vp/Vs of the accreted sediment is relatively low. We consider that this decrease in Vp/Vs reflects consolidation because of mechanical compaction under tectonic loading.

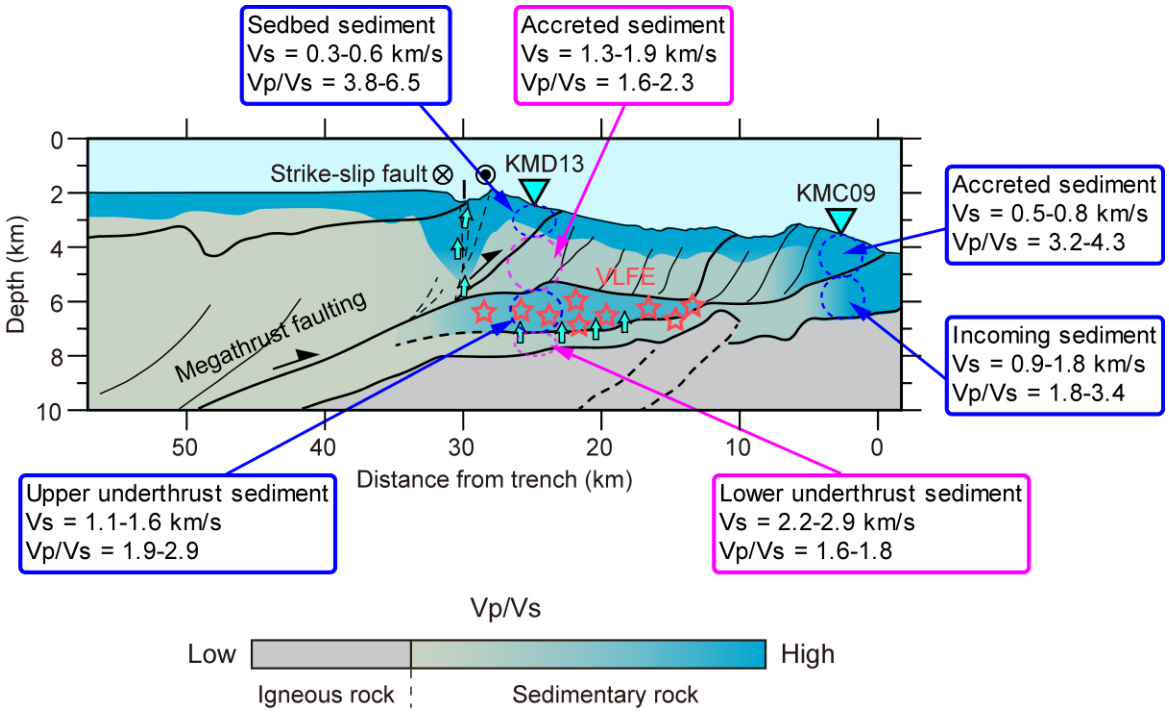

Figure 4 Schematic illustration of our interpretations. The background color indicates the interpolation and extrapolation of Vp/Vs obtained in this study. The 95% confidence intervals of Vs and Vp/Vs are shown for each geological unit. The orange stars represent very-low-frequency earthquakes. The sky-blue arrows depict fluid flow.

A remarkable finding is the LVZ within the upper portion of the underthrust sediment. Although a similar LVZ has been previously reported based on Vp information (Kamei et al., 2013; Park et al., 2010; see Figure S1), our results clarify that the overpressured zone (i.e., the high Vp/Vs zone) localizes within only the upper portion of the underthrust sediment, right above the décollement. This zone between the décollement and the base of accreted sediment was interpreted as shear zone in previous study (Tsuji, Kamei et al., 2014). Fluids may be trapped in this portion with the aid of the permeability barrier by compacted but still well stratified accretionary sediment above. In contrast, the lower underthrust thrust sediment is considered dewatered in light of its relatively high Vs and low Vp/Vs. Mechanical compaction and metamorphic dehydration (J. C. Moore & Saffer, 2001) may squeeze fluid from the lower underthrust sediment, and the fluid may ascend to the upper part, contributing to the fluid-rich condition.

The LVZ in the underthrust sediment invokes the widely accepted idea that slow earthquakes, including VLFEs, occur where pore fluid pressure is high (Saffer & Wallace, 2015). Following this notion, we consider that VLFEs in this region most likely to occur within the upper portion of the underthrust sediment, where we infer high pore pressure. Notably, the VLFE region bounds on the 1944 Tonankai earthquake's rupture zone (Figure 1a). Strain release by the intense VLFE activities may impede the coseismic rupture propagation further updip into the

VLFE region. Instead, the rupture may propagate along the splay fault (Baba et al., 2006). Furthermore, the fluid-rich underthrust sediment beneath the outer ridge may weaken the strength of the hanging wall such that strike-slip motion along the outer ridge (Tsuji, Ashi, et al., 2014) can occur (Figure 4). The Vp model of Kamei et al. (2013) supports this idea in that it predicts a low Vp zone near the strike-slip fault. The strain partitioning due to this strike-slip motion could be another key factor that impedes the rupture propagation.

This study shows the possibility of receiver function analysis as a new tool to study fluid-related heterogeneities in subduction forearcs; our method can provide unique constraints on Vs (or Vp/Vs) with a comparable resolution to that of active-source surveys. Seismometer instrumentation on the seafloor has become popular worldwide. Future applications of our method to such offshore seismometer networks (or more dense deployments in the near future) await.

Acknowledgment

We thank Rie Nakata (Kamei) for providing the velocity model. This study was supported by JSPS KAKENHI Grant Numbers JP16H06472, JP16H06475, JP19K14811, and JP19K21892. Waveform data of DONET1 stations are available on the web page of National Research Institute for Earth Science and Disaster Resilience (https://doi.org/10.17598/nied.0008). The computer programs of MCD and MCMC inversion are available at the Zenodo web page (https://doi.org/10.5281/zenodo.2548974, and https://doi.org/10.5281/zenodo.3663089, respectively). Hypocenters of VLFEs were downloaded from Slow Earthquake Database (Kano et al., 2018; http://www-solid.eps.s.u-tokyo.ac.jp/~sloweq).

References

Agostinetti, N. P., & Malinverno, A. (2010). Receiver function inversion by trans-dimensional Monte Carlo sampling. *Geophysical Journal International*, *181*(2), 858–872. https://doi.org/10.1111/j.1365-246X.2010.04530.x

Akuhara, T., Mochizuki, K., Kawakatsu, H., & Takeuchi, N. (2016). Non-linear waveform analysis for water-layer response and its application to high-frequency receiver function analysis using OBS array. *Geophysical Journal International*, *206*(3), 1914–1920. https://doi.org/10.1093/gji/ggw253

Akuhara, T., Mochizuki, K., Kawakatsu, H., & Takeuchi, N. (2017). A fluid-rich layer along the Nankai trough megathrust fault off the Kii Peninsula inferred from receiver function inversion. *Journal of Geophysical Research: Solid Earth*, *122*(8), 6524–6537. https://doi.org/10.1002/2017JB013965

Akuhara, T., Bostock, M. G., Plourde, A. P., & Shinohara, M. (2019). Beyond Receiver Functions: Green's Function Estimation by Transdimensional Inversion and Its Application to OBS Data. *Journal of Geophysical Research: Solid Earth*, *124*(2), 1944–1961. https://doi.org/10.1029/2018JB016499

Ando, M. (1975). Source mechanisms and tectonic significance of historical earthquakes along the nankai trough, Japan. *Tectonophysics*, *27*(2), 119–140. https://doi.org/10.1016/0040-1951(75)90102-X

Araki, E., Saffer, D. M., Kopf, A. J., Wallace, L. M., Kimura, T., Machida, Y., et al. (2017). Recurring and triggered slow-slip events near the trench at the Nankai Trough subduction megathrust. *Science*. https://doi.org/10.1126/science.aan3120

Baba, T., Cummins, P. R., Hori, T., & Kaneda, Y. (2006). High precision slip distribution of the 1944 Tonankai earthquake inferred from tsunami waveforms: Possible slip on a splay fault. *Tectonophysics*, *426*(1–2), 119–134. https://doi.org/10.1016/j.tecto.2006.02.015

Bangs, N. L. B., Moore, G. F., Gulick, S. P. S., Pangborn, E. M., Tobin, H. J., Kuramoto, S., & Taira, A. (2009). Broad, weak regions of the Nankai Megathrust and implications for shallow coseismic slip. *Earth and Planetary Science Letters*, *284*(1–2), 44–49. https://doi.org/10.1016/j.epsl.2009.04.026

Bell, R., Sutherland, R., Barker, D. H. N., Henrys, S., Bannister, S., Wallace, L., & Beavan, J. (2010). Seismic reflection character of the Hikurangi subduction interface, New Zealand, in the region of repeated Gisborne slow slip events. *Geophysical Journal International*, *180*(1), 34–48. https://doi.org/10.1111/j.1365-246X.2009.04401.x

Bodin, T., Sambridge, M., Tkalćić, H., Arroucau, P., Gallagher, K., & Rawlinson, N. (2012). Transdimensional inversion of receiver functions and surface wave dispersion. *Journal of Geophysical Research: Solid Earth*, *117*(2), 1–24. https://doi.org/10.1029/2011JB008560

Brocher, T. M. (2005). Empirical relations between elastic wavespeeds and density in the Earth's crust. *Bulletin of the Seismological Society of America*, *95*(6), 2081–2092. https://doi.org/10.1785/0120050077

Canales, J. P., Carbotte, S. M., Nedimovic, M. R., & Carton, H. (2017). Dry Juan de Fuca slab revealed by quantification of water entering Cascadia subduction zone. *Nature Geoscience*. https://doi.org/10.1038/NGEO3050

Christensen, I. (1978). Ophiolites, structure seismic velocities and oceanic crustal. *Program*, *47*, 131–157.

Dvorkin, J., Mavko, G., & Nur, A. (1999). Overpressure detection from compressional- and shear-wave data. *Geophysical Research Letters*. https://doi.org/10.1029/1999GL008382

Gray, M., Bell, R. E., Morgan, J. V., Henrys, S., & Barker, D. H. N. (2019). Imaging the Shallow Subsurface Structure of the North Hikurangi Subduction Zone, New Zealand, Using 2-D Full-Waveform Inversion. *Journal of Geophysical Research: Solid Earth*. https://doi.org/10.1029/2019JB017793

Green, P. J. (1995). Reversible jump Markov chain monte carlo computation and Bayesian model determination. *Biometrika*, *82*(4), 711–732. https://doi.org/10.1093/biomet/82.4.711

Hamilton, E. L. (1979). V_p / V_s and Poisson's ratios in marine sediments and rocks. *The Journal of the Acoustical Society of America*, *66*(4), 1093–1101. https://doi.org/10.1121/1.383344

Ito, Y., & Obara, K. (2006). Very low frequency earthquakes within accretionary prisms are very low stress-drop earthquakes. *Geophysical Research Letters*. https://doi.org/10.1029/2006GL025883

Kamei, R., Pratt, R. G., & Tsuji, T. (2012). Waveform tomography imaging of a megasplay fault system in the seismogenic Nankai subduction zone. *Earth and Planetary Science Letters*, *317–318*, 343–353. https://doi.org/10.1016/j.epsl.2011.10.042

Kamei, R., Pratt, R. G., & Tsuji, T. (2013). On acoustic waveform tomography of wide-angle OBS data-strategies for pre-conditioning and inversion. *Geophysical Journal International*, *194*(2), 1250–1280. https://doi.org/10.1093/gji/ggt165

Kikuchi, M., Nakamura, M., & Yoshikawa, K. (2003). Source rupture processes of the 1944 Tonankai earthquake and the 1945 Mikawa earthquake derived from low-gain seismograms. *Earth, Planets and Space*. https://doi.org/10.1186/BF03351745

Kimura, G., Hina, S., Hamada, Y., Kameda, J., Tsuji, T., Kinoshita, M., & Yamaguchi, A. (2012). Runaway slip to the trench due to rupture of highly pressurized megathrust beneath the middle trench slope: The tsunamigenesis of the 2011 Tohoku earthquake off the east coast of northern Japan. *Earth and Planetary Science Letters*, *339–340*, 32–45. https://doi.org/10.1016/j.epsl.2012.04.002

Kitajima, H., & Saffer, D. M. (2012). Elevated pore pressure and anomalously low stress in regions of low frequency earthquakes along the Nankai Trough subduction megathrust. *Geophysical Research Letters*. https://doi.org/10.1029/2012GL053793

Langston, C. A. (1979). Structure under Mount Rainier, Washington, inferred from teleseismic body waves. *Journal of Geophysical Research*, *84*(B9), 4749–4762. https://doi.org/10.1029/JB084iB09p04749

Li, J., Shillington, D. J., Bécel, A., Nedimović, M. R., Webb, S. C., Saffer, D. M., et al. (2015). Downdip variations in seismic reflection character: Implications for fault structure and seismogenic behavior in the Alaska subduction zone. *Journal of Geophysical Research: Solid Earth*. https://doi.org/10.1002/2015JB012338

Ligorría, J. P., & Ammon, C. J. (1999). Iterative deconvolution and receiver-function estimation. *Bulletin of the Seismological Society of America*, *89*(5), 1395–1400.

Moore, G. F., Park, J.-O., Bangs, N. L., Gulick, S. P., Tobin, H. J., Nakamura, Y., et al. (2009). Structural and seismic stratigraphic framework of the NanTroSEIZE Stage 1 transect, *314*. https://doi.org/10.2204/iodp.proc.314315316.102.2009

Moore, J. C., & Saffer, D. (2001). Updip limit of the seismogenic zone beneath the accretionary prism of Southwest Japan: An effect of diagenetic to low-grade metamorphic processes and increasing effective stress. *Geology*. https://doi.org/10.1130/0091-7613(2001)029<0183:ULOTSZ>2.0.CO;2

Nakanishi, A., Kodaira, S., Miura, S., Ito, A., Sato, T., Park, J. O., et al. (2008). Detailed structural image around splay-fault branching in the Nankai subduction seismogenic zone: Results from a high-density ocean bottom seismic survey. *Journal of Geophysical Research: Solid Earth*, *113*(3), 1–14. https://doi.org/10.1029/2007JB004974

Nakano, M., Hori, T., Araki, E., Takahashi, N., & Kodaira, S. (2016). Ocean Floor Networks Capture Low-Frequency Earthquake Event. *Eos*, *97*. https://doi.org/10.1029/2016EO052877

Nakano, M., Hori, T., Araki, E., Kodaira, S., & Ide, S. (2018). Shallow very-low-frequency earthquakes accompany slow slip events in the Nankai subduction zone. *Nature Communications*, *9*(1), 984. https://doi.org/10.1038/s41467-018-03431-5

Park, J. O., Tsuru, T., Kodaira, S., Cummins, P. R., & Kaneda, Y. (2002). Splay fault branching along the Nankai subduction zone. *Science*, *297*(5584), 1157–1160. https://doi.org/10.1126/science.1074111

Park, J. O., Fujie, G., Wijerathne, L., Hori, T., Kodaira, S., Fukao, Y., et al. (2010). A low-velocity zone with weak reflectivity along the Nankai subduction zone. *Geology*, *38*(3), 283–286. https://doi.org/10.1130/G30205.1

Ruan, Y., Forsyth, D. W., & Bell, S. W. (2014). Marine sediment shear velocity structure from the ratio of displacement to pressure of Rayleigh waves at seafloor. *Journal of Geophysical Research: Solid Earth*. https://doi.org/10.1002/2014JB011162

Saffer, D. M., & Wallace, L. M. (2015). The frictional, hydrologic, metamorphic and thermal habitat of shallow slow earthquakes. *Nature Geoscience*, *8*(8), 594–600. https://doi.org/10.1038/ngeo2490

Sambridge, M. (2014). A Parallel Tempering algorithm for probabilistic sampling and multimodal optimization. *Geophysical Journal International*, *196*(1), 357–374. https://doi.org/10.1093/gji/ggt342

Scholz, C. H. (1998). Earthquakes and friction laws. *Nature*, *391*(6662), 37–42. https://doi.org/10.1038/34097

Shiraishi, K., Moore, G. F., Yamada, Y., Kinoshita, M., Sanada, Y., & Kimura, G. (2019). Seismogenic Zone Structures Revealed by Improved 3-D Seismic Images in the Nankai Trough off Kumano. *Geochemistry, Geophysics, Geosystems*, *20*(5), 2252–2271. https://doi.org/10.1029/2018GC008173

Sugioka, H., Okamoto, T., Nakamura, T., Ishihara, Y., Ito, A., Obana, K., et al. (2012). Tsunamigenic potential of the shallow subduction plate boundary inferred from slow seismic slip. *Nature Geoscience*, *5*(6), 414–418. https://doi.org/10.1038/ngeo1466

Takemura, S., Matsuzawa, T., Kimura, T., Tonegawa, T., & Shiomi, K. (2018). Centroid Moment Tensor Inversion of Shallow Very Low Frequency Earthquakes Off the Kii Peninsula, Japan, Using a Three-Dimensional Velocity Structure Model. *Geophysical Research Letters*. https://doi.org/10.1029/2018GL078455

Thomson, W. T. (1950). Transmission of elastic waves through a stratified medium. *Journal of Applied Physics*, *21*(1950), 89–93; 89.

To, A., Obana, K., Sugioka, H., Araki, E., Takahashi, N., & Fukao, Y. (2015). Small size very low frequency earthquakes in the Nankai accretionary prism, following the 2011 Tohoku-Oki earthquake. *Physics of the Earth and Planetary Interiors*. https://doi.org/10.1016/j.pepi.2015.04.007

Tonegawa, T., Araki, E., Kimura, T., Nakamura, T., Nakano, M., & Suzuki, K. (2017). Sporadic low-velocity volumes spatially correlate with shallow very low frequency earthquake clusters. *Nature Comm.*, *8*(2048), 1–7. https://doi.org/10.1038/s41467-017-02276-8

Tsuji, T., Dvorkin, J., Mavko, G., Nakata, N., Matsuoka, T., Nakanishi, A., et al. (2011). V P / V S ratio and shear-wave splitting in the Nankai Trough seismogenic zone: Insights into effective stress, pore pressure, and sediment consolidation. *Geophysics*, *76*(3), WA71-WA82. https://doi.org/10.1190/1.3560018

Tsuji, T., Kamei, R., & Pratt, R. G. (2014). Pore pressure distribution of a mega-splay fault system in the Nankai trough subduction zone: Insight into up-dip extent of the seismogenic zone. *Earth and Planetary Science Letters*, *396*, 165–178. https://doi.org/10.1016/j.epsl.2014.04.011

Tsuji, T., Ashi, J., & Ikeda, Y. (2014). Strike-slip motion of a mega-splay fault system in the Nankai oblique subduction zone. *Earth, Planets and Space*, *66*(1), 120. https://doi.org/10.1186/1880-5981-66-120

Geophysical Research Letters

Supporting Information for

Overpressured underthrust sediment in the Nankai Trough forearc inferred from high-frequency receiver function inversion

Takeshi Akuhara[1], Takeshi Tsuji[2], and Takashi Tonegawa[3]

[1]Earthquake Research Institute, The University of Tokyo, [2]Department of Earth Resources Engineering, Kyushu University, [3]Research Institute for Marine Geodynamics, JAMSTEC

Contents of this file

Introduction

This supporting information provides: details of the transdimensional Markov-chain Monte Carlo inversion (Text S1); P-wave velocity models by previous studies (Figures S1); procedure of Green's function selection (Figure S2); inversion retuls that are not shown in the main text (Figures S3–5); and lists of tuning parameters for the inversion analysis (Tables S1–2).

Text S1. Transdimensional Markov-chain Monte Carlo inversion

The transdimensional Markov-chain Monte Carlo (MCMC) inversion estimates the posterior probability of k and $\mathbf{m}_k = (z_1 \cdots z_k, \delta\alpha_1 \cdots \delta\alpha_{k+1}, \delta\beta_1 \cdots \delta\beta_{k+1})^{\mathrm{T}}$ with the given input data, $\mathbf{d}$, as follows:

$$P(k, \mathbf{m}_k|\mathbf{d}) \propto P(k)P(\mathbf{m}_k|k)P(\mathbf{d}|k, \mathbf{m}_k)$$
$$= P(k)\prod_{i=1}^{k}\{P(z_i)\}\prod_{i=1}^{k+1}\{P(\delta\alpha_i)\}\prod_{i=1}^{k+1}\{P(\delta\beta_i)\}\,P(\mathbf{d}|k, \mathbf{m}_k), \#(S1)$$

where $P(x|y)$ represents the probability to realize x with y given, and $P(x)$ is a prior probability of x. The other notations are defined in Section 3 of the main text.

As the prior probabilities for k and z_i, we assume truncated uniform priors bounded from k_{min} to k_{max} and from z_{min} to z_{max}, respectively:

$$P(k) = \begin{cases} \dfrac{1}{k_{max} - k_{min}} & (k_{min} \le k < k_{max}) \\ 0 & (\text{otherwise}) \end{cases} \#(S2)$$

and

$$P(z_i) = \begin{cases} \dfrac{1}{z_{max} - z_{min}} & (z_{min} \le z_i \le z_{max}) \\ 0 & (\text{otherwise}) \end{cases}. \#(S3)$$

For the velocity anomalies, we assume Gaussian priors with zero-mean and standard deviations of $\sigma_{\delta\alpha}$ and $\sigma_{\delta\beta}$ as follows:

$$P(\delta\alpha_i) = \frac{1}{\sqrt{2\pi\sigma_{\delta\alpha}^2}}\exp\left(-\frac{\delta\alpha_i^2}{2\sigma_{\delta\alpha}^2}\right), \#(S4)$$

and

$$P(\delta\beta_i) = \frac{1}{\sqrt{2\pi\sigma_{\delta\beta}^2}}\exp\left(-\frac{\delta\beta_i^2}{2\sigma_{\delta\beta}^2}\right). \#(S5)$$

Here, k_{min}, k_{max}, z_{min}, z_{max}, $\sigma_{\delta\alpha}$, and $\sigma_{\delta\beta}$ are parameters selected in accordance with prior knowledge. The values used in this study are summarized in Table S1.

With a given model, $\mathbf{m}_k$, synthetic GF, $\mathbf{g}(k, \mathbf{m}_k)$, is computed using the propagator matrix method (Thomson, 1950). Then, the likelihood, $P(\mathbf{d}|k, \mathbf{m}_k)$, can be calculated as follows:

$$P(\mathbf{d}|k,\mathbf{m}_k) = \frac{1}{\sqrt{(2\pi)^N|\mathbf{C}|}}\exp\left[-\frac{1}{2}\{\mathbf{g}(k,\mathbf{m}_k)-\mathbf{d}\}^{\mathrm{T}}\mathbf{C}^{-1}\{\mathbf{g}(k,\mathbf{m}_k)-\mathbf{d}\}\right], \#(S6)$$

where $\mathbf{C}$ is the covariance matrix, and N is the number of elements in the time series. Following Bodin et al. (2012), we parameterize the covariance matrix by $C_{ij} = \sigma^2 r^{(j-i)^2}$, in which σ denotes a standard deviation of data noise, and r denotes the noise temporal correlation. Both parameters are time-invariant and fixed during the inversion. We fix σ at ~0.02 based on the time-averaged standard errors obtained during the GF stacking. The temporal correlation r is associated with the low-pass filter by $r = e^{-(a\Delta t)^2}$, where a is a parameter of the low-pass filter and Δt is a waveform sampling interval.

For each iteration step, a new model is proposed by slightly modifying the current model. We allow five types of proposals: (1) adding a new layer interface; (2) removing a layer interface; and perturbing the (3) layer interface depth, (4) Vp anomaly, and (5) Vs anomaly. The amount of perturbation is randomly extracted from a normal distribution with a certain standard deviation (Table S2). After calculating the likelihood, the proposed model is accepted or rejected in accordance with the Metropolis-Hastings-Green criterion (Green, 1995). Irrespective of this criterion, we reject proposals of an anomalous layer with low Vp (<0.1 km/s), Vs (<0.0 km/s) or Vp/Vs (< 1.5), or high Vp (>8.6 km/s), Vs (>5.0 km/s) or Vp/Vs (>7.0). This additional condition may be regarded as another class of prior beyond the description of Equations S2–S5.

The aforementioned iteration is repeated 5×10^5 times; however models sampled during the first 2.5×10^5 iterations are not saved to eliminate initial sample dependency (termed the burn-in period). Even after the burn-in period, we only save the model once every 100 iterations to avoid artificial correlation with the previous samples. Furthermore, we employ the parallel tempering technique (Sambridge, 2014), in which 100 MCMC sampling processes run in parallel. Out of the 100 processes, 80 are tempered with different temperatures: The acceptance criterion is modified in response to the temperature such that higher temperature processes can more frequently accept proposals. The remaining 20 processes are given a unit temperature and used to estimate the posterior probability. At every iteration, the temperature may be swapped between processes, allowing a long jump in the model space. In this manner, we finally construct the posterior probability from a total of 5×10^4 models.

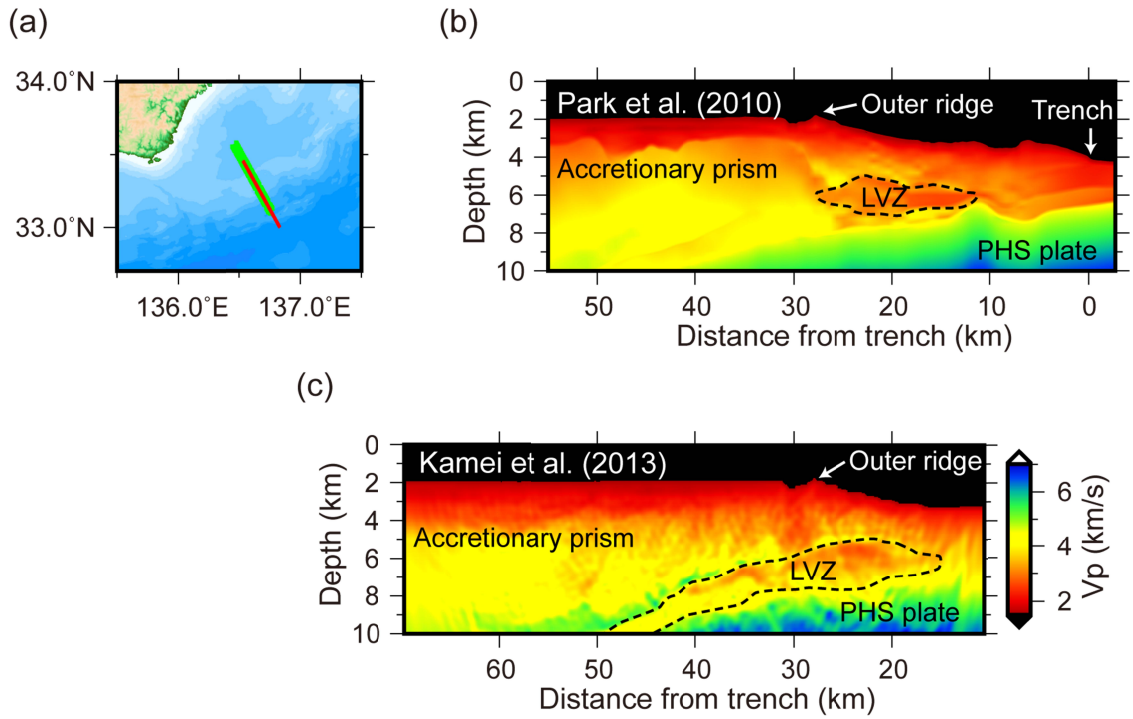

Figure S1. P-wave velocity (Vp) models by previous studies. (a) The profile locations of the Vp models by Park et al. (2010) and Kamei et al. (2013), which are shown by the green and red lines, respectively. (b) The Vp model by Park et al. (2010). (c) The Vp model by Kamei et al. (2013). LVZ = low-velocity zone; PHS = Philippine Sea.

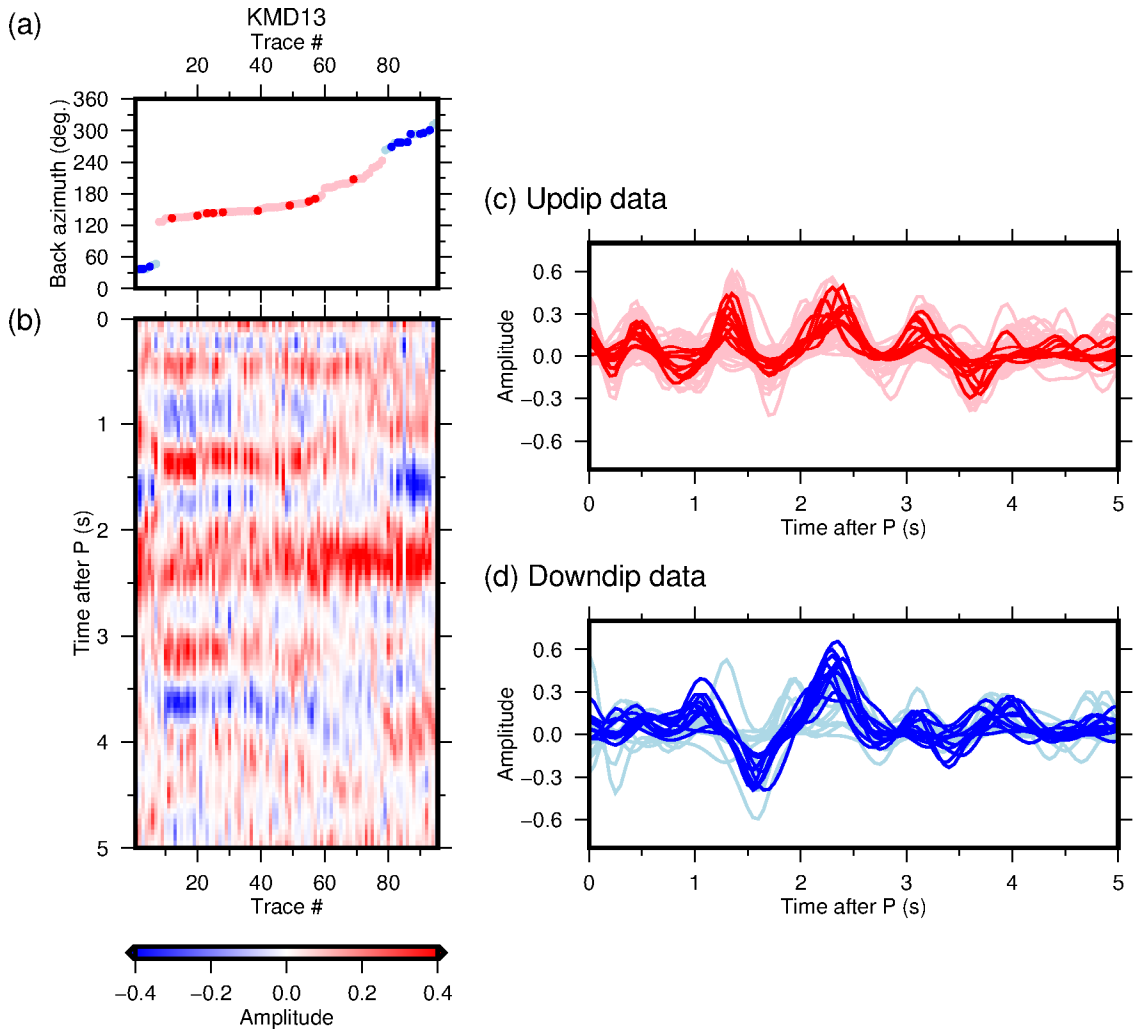

Figure S2. Green's functions (GFs) calculated for KMD13. (a) Back azimuth of each GF shown in (b). Red and blue dots represent the updip and downdip data, respectively. Those selected for the inputs to the inversion analysis is shown in bright colors, while the others in pale colors. (b) GF amplitudes are shown in red (positive) and blue (negative) colors. (c-d) GFs included in (c) the updip and (d) downdip subsets. The color notation is the same as (a).

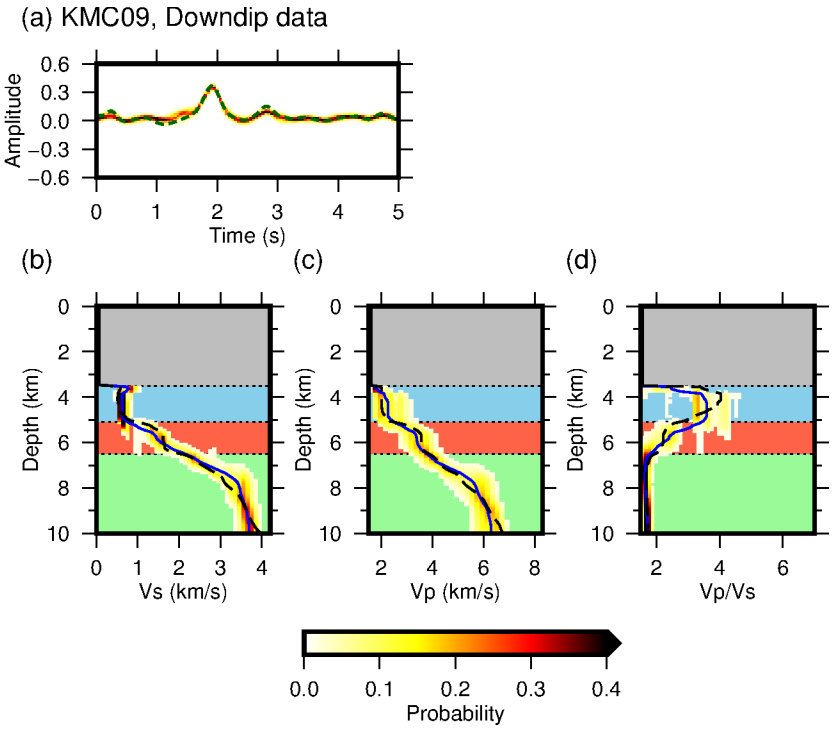

Figure S3. Results of inversion analysis for KMC09 with the downdip data. The notations are the same as Figure 2 in the main text except that the mean model from the updip data is shown by dashed lines for comparison.

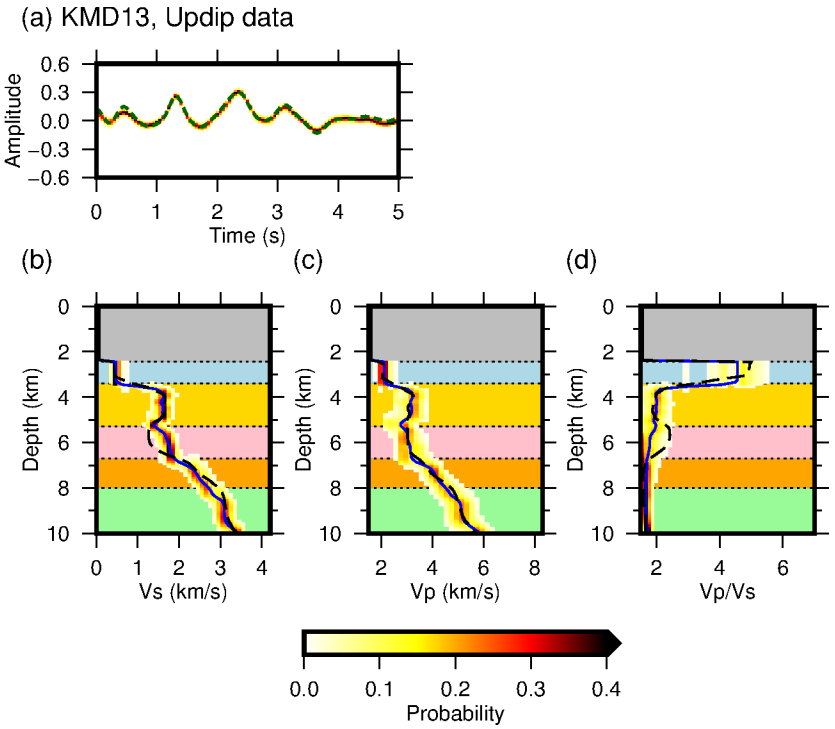

Figure S4. Results of inversion analysis for KMD13 with the updip data. The notations are the same as Figure 2 in the main text except that the mean model from the downdip data is shown by dashed lines for comparison.

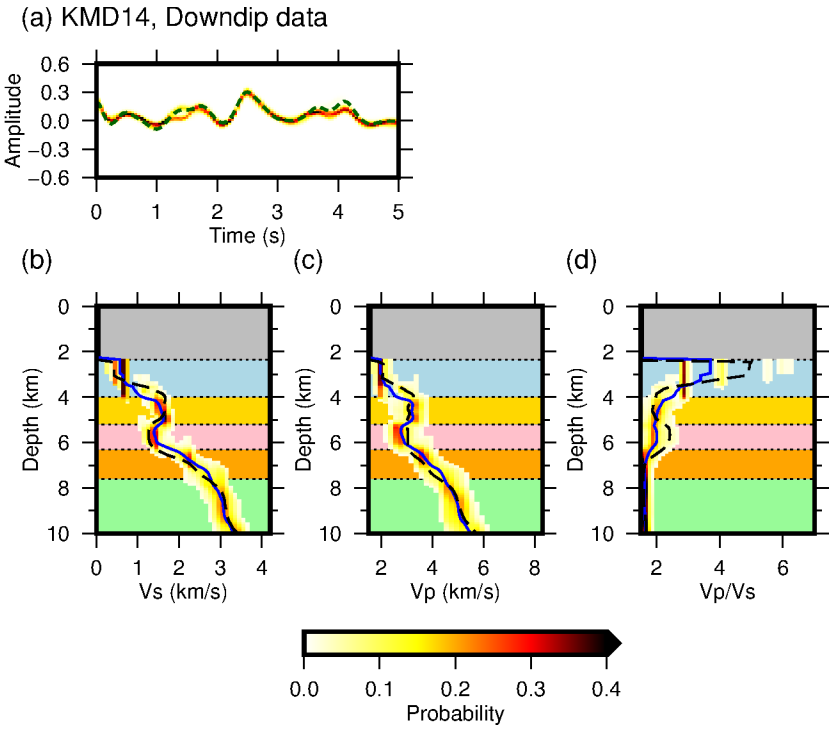

Figure S5. Results of inversion analysis for KMD14 with the downdip data. The notations are the same as Figure 2 in the main text except that the mean model from KMD13 (downdip data) is shown by dashed lines for comparison.

Table S1. Parameter choice for the prior probabilities.

Parameter	Value used in this study
k_{min}	1
k_{max}	21
z_{min}	Station level
z_{max}	10 km
$\sigma_{\delta\alpha}$	0.2 km/s
$\sigma_{\delta\beta}$	0.1 km/s

Table S2. Parameter choice for proposals.

Parameter	Value used in this study
Standard deviation for perturbing z_i	0.02 km
Standard deviation for perturbing $\delta\alpha_i$	0.03 km/s
Standard deviation for perturbing $\delta\beta_i$	0.03 km/s